Experimental results on wavefront correction using the self-coherent camera

M. Mas, P. Baudoz, Johan Mazoyer, R. Galicher, G. Rousset

Experimental results on wavefront correction using the self-coherent camera

M. Mas, P. Baudoz, J. Mazoyer, R. Galicher, G. Rousset

M. Mas, P. Baudoz, J. Mazoyer, R. Galicher, G. Rousset, "Experimental results on wavefront correction using the self-coherent camera," Proc. SPIE 8446, Ground-based and Airborne Instrumentation for Astronomy IV, 844689 (24 September 2012); doi: 10.1117/12.926586

SPIE.

Event: SPIE Astronomical Telescopes + Instrumentation, 2012, Amsterdam, Netherlands

Experimental results on wavefront correction using the self-coherent camera

Mas, M.[a,b], Baudoz, P.[b], Mazoyer, J.[b], Galicher, R.[c,d] and Rousset, G.[b]

[a]Laboratoire d'Astrophysique de Marseille, CNRS-INSU, Université d'Aix-Marseille, 38 rue Frédéric Joliot-Curie, 13388 Marseille cedex 13 France;
[b]LESIA, Observatoire de Paris, CNRS, Université Pierre et Marie Curie Paris 6 and Université Denis Diderot Paris 7, 5 place Jules Janssen, 92195 Meudon, France;
[c]National Research Council Canada, Herzberg Institute of Astrophysics, 5071 West Saanich Road, Victoria, BC, V9E 2E7, Canada;
[d]Dept. de Physique, Université de Montréal, C.P. 6128 Succ. Centre-ville, Montréal, Qc, H3C 3J7, Canada;

ABSTRACT

The Self-Coherent Camera is dedicated to the direct detection of exoplanets. This instrument can be used as a focal plane wavefront sensor to measure static aberrations that induce speckles on the detector, which prevents the detection of faint companions. The Self-Coherent Camera creates a reference beam in the Lyot stop pupil plane in order to spatially modulate the speckle pattern with Fizeau fringes. We can then estimate for wavefront aberrations upstream of the coronagraphic mask and correct for them using a deformable mirror. Currently, the Self-Coherent Camera is combined with a deformable mirror located in the pupil plane upstream of a Four-Quadrant Phase Mask Coronagraph.

In this paper, we present the formalism that explains how the Self-Coherent Camera encodes speckles and how we estimate the wavefront aberrations directly from the science image. We present numerical simulation results on speckle suppression in the focal plane. Then, we give experimental results on wavefront correction on our optical bench using a 32x32 actuators deformable mirror. We show that we can improve the contrast in the focal plane by a factor of more than 100 in the PSF wings up to $12\lambda/D$.

Keywords: Instrumentation, high contrast imaging, high angular resolution, coronagraphy, wavefront correction

1. INTRODUCTION

More than 700 exoplanets have already been detected since 1995. Most of them were discovered using indirect detections. These methods provide information on geometrical parameters of the planet and of the orbit. Direct imaging is required to study intrinsic parameters like temperature and chemical composition of the exoplanet atmosphere. Such detections can require contrasts as high as 10^9-10^{10} in visible light and high angular resolution. Extreme adaptive optics and coronagraphy can be combined to reach such high contrast. Nevertheless, small optical aberrations in the instrument degrade the coronagraph performance and speckles are recorded in the final focal plane. These speckles are brighter than the image of the companion and have the same size and shape. We propose to use a Self-Coherent Camera (SCC) as a focal plane wavefront sensor to estimate static aberrations upstream of a Four-Quadrant Phase Mask (FQPM) coronagraph. Then, the instrumental aberrations are corrected with a deformable mirror in order to reduce the speckle noise in the final focal plane.

In section 2, we recall the principle of the SCC[1–4] which uses the coherence between the rejected stellar light and the residual stellar light to encode speckles in the final focal plane. We then develop the formalism to estimate phase and amplitude aberrations upstream of the coronagraph in section 3. To validate this formalism, we present results of numerical simulations on phase and amplitude correction in section 4. In this section,

Further author information: (Send correspondence to Marion Mas)
E-mail: marion.mas@oamp.fr, Telephone: +33 (0)4 91 05 59 24

Ground-based and Airborne Instrumentation for Astronomy IV, edited by Ian S. McLean, Suzanne K. Ramsay, Hideki Takami, Proc. of SPIE Vol. 8446, 844689 · © 2012 SPIE · CCC code: 0277-786X/12/$18 · doi: 10.1117/12.926586

we first expose the method to create the interaction matrix of the system, then we show numerical results on speckle suppression. In section 5, we present the optical bench we developed at LESIA. Eventually, we present experimental results on wavefront estimation and correction using the SCC coupled with a FQPM and an electrostatic Boston Micromachines deformable mirror with 32x32 actuators.

2. SCC PRINCIPLE

2.1 Presentation

We present in this section the principle of the SCC. Figure 1 is a schematic representation of the SCC combined with a FQPM coronagraph and a deformable mirror. The stellar light is collected by the telescope and goes through the entrance pupil P. This light is affected by the FQPM focal mask M in the next focal plane. Hence, the non-aberrated part of the stellar light is rejected outside of the geometrical pupil in the next pupil plane and is stopped by the Lyot stop diaphragm L. The aberrated part of the beam that induces speckles and the light coming from a companion go through the Lyot stop, called *image channel*. Speckles are then recorded on the detector in the finale focal plane (Figure 2, left). To calibrate these speckles, we add a small hole in the Lyot stop to create *a reference channel* R. It selects only part of the stellar that is rejected by the coronagraph. The two beams are recombined in the focal plane in Fizeau fringes. As the companion light and stellar light are not coherent, the reference light interferes only with the speckles (Figure 2, right). In the following, we call *SCC image* the image in the focal plane of encoded speckles. From these encoded speckles, it is possible to estimate aberrations upstream of the coronagraph in the entrance pupil (see section 3). The contrast of the fringes depends on the reference size and position, a dedicated study on the reference is developed in Mazoyer et al., 2012.[5]

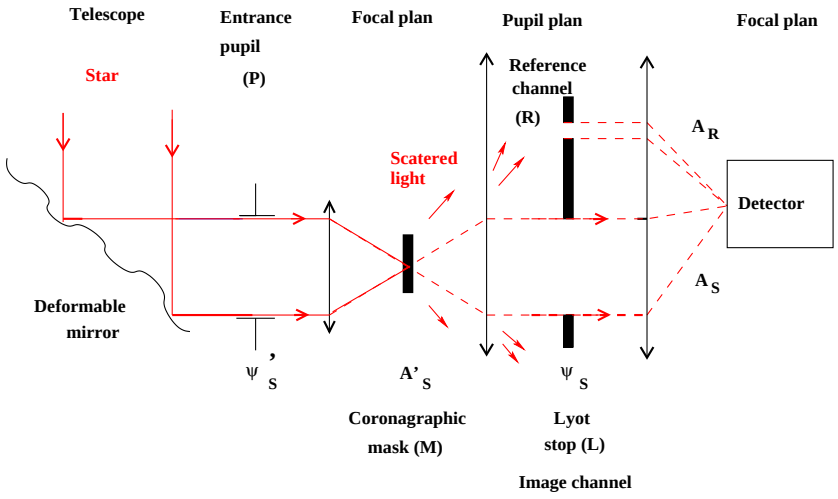

Figure 1. Principle of the SCC coupled with a FQPM coronagraph and a deformable mirror. A small hole is added in the Lyot stop pupil plane to create a reference. In the final focal plane, speckles are encoded with Fizeau fringes.

2.2 Image formation with the SCC

We develop in this section the formalism to write the intensity of encoded speckles in the focal plane. We assume that the star is a punctual monochromatic source centered on the optical axis. We note α the amplitude and ϕ the phase of the aberrations in the entrance pupil noted P (first pupil plane upstream of the coronagraph). The complex amplitude of the star, in this plane is ψ'_S and can be written as:

$$\psi'_S(\vec{\xi}) = \psi_0 \, P(\vec{\xi}) \, \exp\left(\alpha(\vec{\xi}) + i\phi(\vec{\xi})\right) \tag{1}$$

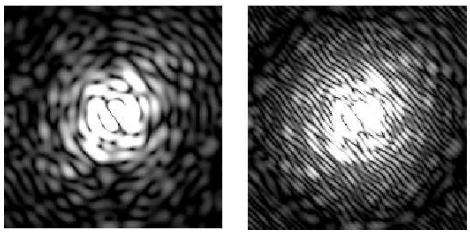

Figure 2. Numerical simulations. Phase errors in the entrance pupil ϕ : 20nm rms, no amplitude aberrations ($\alpha = 0$). Left: Speckle field induced in the focal plane. Right: Encoded speckles with the SCC (SCC image) in the focal plane.

ψ_0 is the mean amplitude of the field, $\vec{\xi}$ is the coordinate in pupil plane. We assume that aberrations are small and defined in the pupil P, hence, we can write:

$$\psi'_S = \psi_0 \left(P + \alpha + i\phi\right) \tag{2}$$

The complex amplitude of the residual phase A'_S behind the coronagraphic mask M in the first focal plane is:

$$A'_S(\vec{x}) = \mathcal{F}(\psi'_S)(\vec{x})\, M(\vec{x}) \tag{3}$$

with $\vec{x}$ the coordinate in the focal plane. Using Equation 2, we can write the electric field $\mathcal{F}^{-1}(A'_E)$ before the Lyot stop:

$$\mathcal{F}^{-1}(A'_S) = \psi_0(P + \alpha + i\phi) * \mathcal{F}^{-1}(M) \tag{4}$$

with $*$ the convolution product. After the Lyot stop, the electric field ψ_S is:

$$\psi_S = \psi_0 \left[(P + \alpha + i\phi) * \mathcal{F}^{-1}(M)\right] L \tag{5}$$

We assume a perfect FQPM coronagraph with infinite field. In the case of a point source that is centered on the focal plane mask with no optical aberration, the electric field in the pupil plane after the coronograph is null inside the pupil:[6]

$$\left[P * \mathcal{F}^{-1}(M)\right] P = 0 \tag{6}$$

The electric field ψ_S after the Lyot stop can then also be written:

$$\psi_S = \psi_0[(\alpha + i\phi) * \mathcal{F}^{-1}(M)]\, L \tag{7}$$

We add a small aperture in the Lyot stop plane to create the reference channel R. The reference is shifted by $\vec{\xi_0}$ from the center of the Lyot stop aperture. In order to get fringes in the focal plane and have a good estimation of phase and amplitude aberrations, we set the distance ξ_0 between the two channels as:[3]

$$||\vec{\xi_0}|| > \frac{D_L}{2}\left(3 + \frac{1}{\gamma}\right), \text{ with } \gamma = \frac{D_L}{D_R} \tag{8}$$

with D_L and D_R diameters of the Lyot stop and the reference respectively. The electric field ψ in the Lyot stop plane is:

$$\psi(\vec{\xi}) = \psi_0[(P + \alpha + i\phi) * \mathcal{F}^{-1}(M)].\left(L + R * \delta(\vec{\xi} - \vec{\xi_0})\right) \tag{9}$$

$$\psi(\vec{\xi}) = \psi_S + \psi_R * \delta\left(\vec{\xi} - \vec{\xi_0}\right) \tag{10}$$

The intensity recorded on the detector in the final focal plane is then:

$$I(\vec{x}) = \left|\mathcal{F}(\psi(\vec{\xi}))\right|^2 \tag{11}$$

With A_S and A_R Fourier transform of ψ_S and ψ_R respectively, I can be written as:

$$I(\vec{x}) = |A_S|^2 + |A_R|^2 + 2Re\left(A_S^*\, A_R \exp\left(\frac{2i\pi\vec{x}.\vec{\xi_0}}{\lambda}\right)\right) \tag{12}$$

$$I(\vec{x}) = |A_S|^2 + |A_R|^2 + A_S^*\, A_R \exp\left(\frac{-2i\pi\vec{x}\,\vec{\xi_0}}{\lambda}\right) + A_S\, A_R^* \exp\left(\frac{2i\pi\vec{x}.\vec{\xi_0}}{\lambda}\right) \tag{13}$$

I is the expression of encoded speckles in the focal plane.

Figure 3 represents the steps to follow in order to find an expression of the encoded speckles in the focal plane.

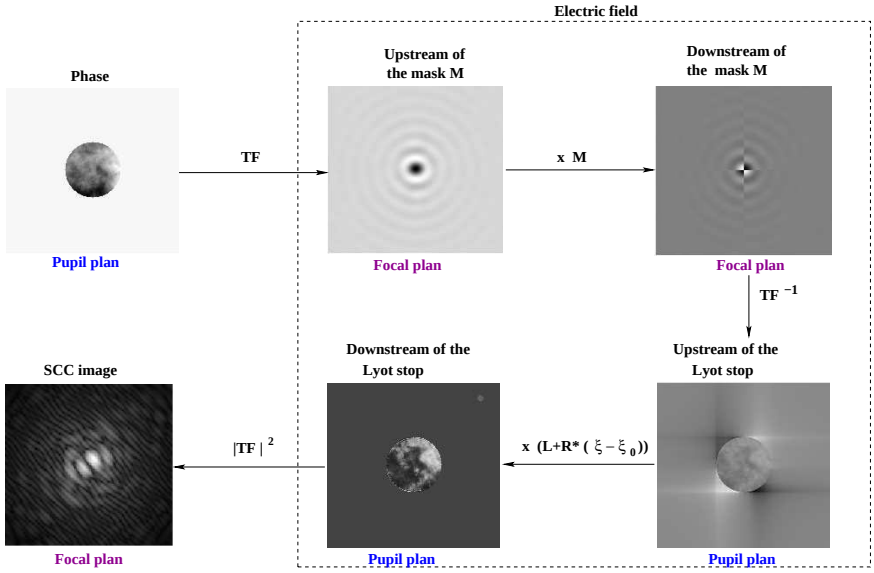

Figure 3. Steps followed in the simulation to calculate electric fields from the phase in the entrance pupil to the encoded speckles in the final focal plane.

3. LINEAR ESTIMATION OF THE WAVEFRONT

SCC images in the focal plane are used to estimate phase and amplitude aberrations upstream of the coronagraph. We present the formalism in this section. We first apply an inverse Fourier transform to the SCC image. With $I_i(\vec{x}) = |A_i(\vec{x})|^2$, we have:

$$\mathcal{F}^{-1}(I) = \mathcal{F}^{-1}(I_S) + \mathcal{F}^{-1}(I_R) + \mathcal{F}^{-1}(A_S^*\, A_R) * \delta(\xi - \xi_0) + \mathcal{F}^{-1}(A_S\, A_R^*) * \delta(\xi + \xi_0) \tag{14}$$

I_S and I_R are the intensities of the star and the reference respectively. Hence, in the correlation plane, we get three peaks (Figure 4). The lateral peaks are conjugated and contain information of the complex amplitude of stellar speckles spatially modulated on the detector. The intensity I_- corresponding to one lateral peak centered in the correlation plane is defined by:

$$\mathcal{F}^{-1}(I_-) = \mathcal{F}^{-1}(A_S\, A_R^*) \tag{15}$$

To find the wavefront errors, we consider the intensity I_-:

$$I_-(\vec{x}) = A_S\, A_R^* \tag{16}$$

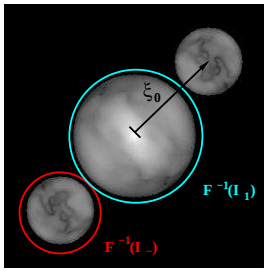

Figure 4. Correlation peaks.

The complex amplitude of the stellar light in the Lyot stop plane is:

$$\psi_S(\vec{\xi}) = \mathcal{F}^{-1}(A_S) \tag{17}$$

$$\psi_S(\vec{\xi}) = \mathcal{F}^{-1}\left(\frac{I_-}{A_R^*}\right) \quad \text{for} \quad A_R^* \quad \neq 0 \tag{18}$$

Using Equation 7, we can write:

$$\frac{\psi_S(\vec{\xi})}{\psi_0} = \mathcal{F}^{-1}\left(\frac{I_-}{\psi_0\, A_R^*}\right) = \left[(\alpha + i\phi) * \mathcal{F}^{-1}(M)\right] L \tag{19}$$

In the following, we consider that there is no amplitude aberrations ($\alpha = 0$) and we note ϕ the phase errors upstream of the coronagraph. The goal is to study the effect on the phase of the convolution of the function $\mathcal{F}^{-1}(M)$ and see if a simple convolution by the function $\mathcal{F}^{-1}(1/M)$ can help us retrieve the phase. This will help us to find a relation between the phase ϕ in the pupil P and the function $\mathcal{F}^{-1}(I_-)$ in order to find an estimation ϕ_{est} of the phase in the pupil plane.

We consider the initial phase ϕ (Figure 5, Image 1):

$$\text{Image } 1 : \phi \tag{20}$$

We then convolve ϕ by the inverse Fourier transform of the mask M (Figure 5, Image 2). The function M is real and symmetric, hence, its inverse Fourier transform is real:

$$\text{Image } 2 : \phi * \mathcal{F}^{-1}(M) \tag{21}$$

Image 2 is then real, we can also notice that very few information is outside of the pupil geometry. This means that most of the spread information from the phase aberration remains in the pupil after the coronagraph. Thus, a Lyot stop at 100% transmission ($L = P$) does not have a strong impact on image 2. We consider a Lyot stop diaphragm at 100% transmission and apply it (Figure 5, Image 3):

$$\text{Image } 3 : \left[\phi * \mathcal{F}^{-1}(M)\right] L \tag{22}$$

Using Equation 7, we can write:

$$\left[\phi * \mathcal{F}^{-1}(M)\, L\right] = Im\left(\frac{\psi_S}{\psi_0}\right) \tag{23}$$

We want to retrieve information in the pupil after the deconvolution by the mask M (Figure 5, Image 4):

$$\text{Image } 4 : \left[\left((\phi * \mathcal{F}^{-1}(M))\, L\right) * \mathcal{F}^{-1}\left(\frac{1}{M}\right)\right] P \tag{24}$$

Theoretically, if no stop is applied in Equation 22 ($L = 1$ everywhere), the "convolution-deconvolution" by the Fourier transform of mask vanishes and the image 4is equal to image 1. Comparing both images, we clearly see

that the filtering by the Lyot stop in the middle of this "reference image"does not distort strongly the phase. Thus, we will use the expression of image 4 as an approximation ϕ_{est} of the phase ϕ.

Using Equation 23, we have:

$$\phi_{est} = \left[\left((\phi * \mathcal{F}^{-1}(M))\, L \right) * \mathcal{F}^{-1}\left(\frac{1}{M}\right) \right] P = \left(Im\left(\frac{\psi_S}{\psi_0}\right) * \mathcal{F}^{-1}\left(\frac{1}{M}\right) \right) P \tag{25}$$

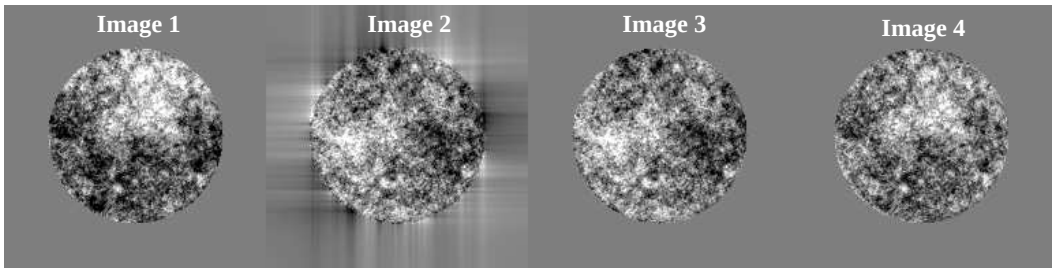

Figure 5. $L = P$ in this case. Image 1: phase ϕ. Image 2: $\phi * \mathcal{F}^{-1}(M)$. Image 3: $(\phi * \mathcal{F}^{-1}(M))\, L$. Image 4: $[((\phi * \mathcal{F}^{-1}(M))\, L) * \mathcal{F}^{-1}(\frac{1}{M})]\, P$.

We can write a linear estimation ϕ_{est} of the phase ϕ upstream of the coronagraph using data provided by the SCC:

$$\phi_{est} = \left[Im\left(\frac{\psi_S}{\psi_0}\right) * \mathcal{F}^{-1}\left(\frac{1}{M}\right) \right] P \tag{26}$$

We get the same results considering amplitude aberrations α. The general equation of the wavefront estimation is then:

$$\alpha_{est} + i\phi_{est} = \mathcal{F}^{-1}\left(\mathcal{F}\left(\frac{\psi_S}{\psi_R}\right) \frac{1}{M} \right) P \tag{27}$$

The reference R has a diameter D_R small enough compared to the Lyot stop diameter D_L to assume that $A_R^* \simeq A_0$ with A_0 a constant equal to the mean of $|A_R|$ on the zone of correction of the deformable mirror in the focal plane. Eventually, we get the linear estimation of the wavefront:

$$\alpha_{est} + i\phi_{est} = \mathcal{F}^{-1}\left(\frac{I_-}{\psi_0\, A_0\, M} \right) P \tag{28}$$

Note that we can divide by M if M is never null as it is the case for a FQPM coronagraph. The steps followed to estimate phase and amplitude aberrations upstream of the coronagraph are summarized in the Figure 6 (in the Figure, we consider that there is no amplitude aberrations).

4. NUMERICAL SIMULATIONS

We validate the formalism presented in the previous section using numerical simulations. The objective is to reproduce the behavior of our high contrast imaging bench (bench *Très Haute Dynamique* THD) in order to draw the parallel between experimental and simulation results. To do so, we simulate the image formation through the instrument, we estimate the aberrations applying the SCC estimator (Equation 28), and we correct for them simulating the action of a deformable mirror. In this section, we present the method used in simulation to create the interaction matrix of the system. This method is also applied on experimental real data taken in the laboratory. Then, we present results of numerical simulations on speckle suppression in the focal plane considering a case similar to the experiment we did in our laboratory. Finally, we show the performance in contrast that we expect after correcting the phase and amplitude upstream of the coronagraph.

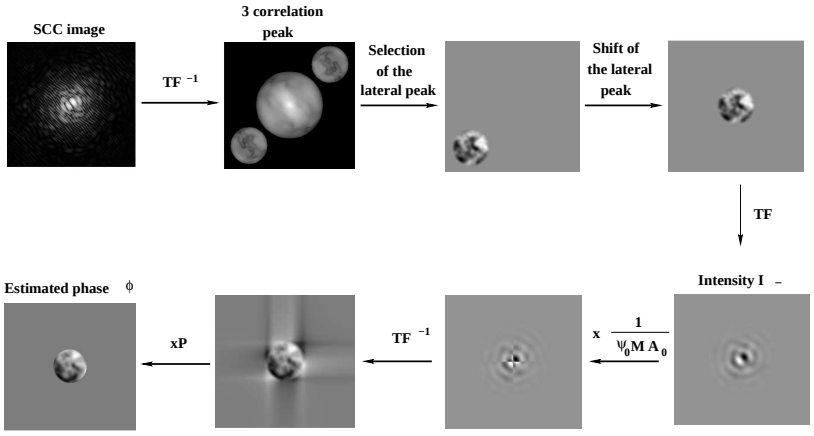

Figure 6. Steps followed to estimate the phase from SCC images.

4.1 Interaction matrix

4.1.1 Influence functions of the deformable mirror

We consider a deformable mirror with NxN actuators ($N = 26$) with a square geometry. We then simulate the influence functions of the deformable mirror:

- We considere a pupil P and we initially define the inter actuator distance as: $D_P/(N-1)$, with D_P the pupil diameter.
- We assume that the deformation of the deformable mirror surface corresponding to the movement of an actuator is a 2D-gaussian function. We call influence function f this deformation (Figure 7):

$$f = c_0 \exp(-U/2) \tag{29}$$
$$U = (x^2 + y^2)/\sigma^2 \tag{30}$$

with c_0 and σ constant, x and y are the coordinates.

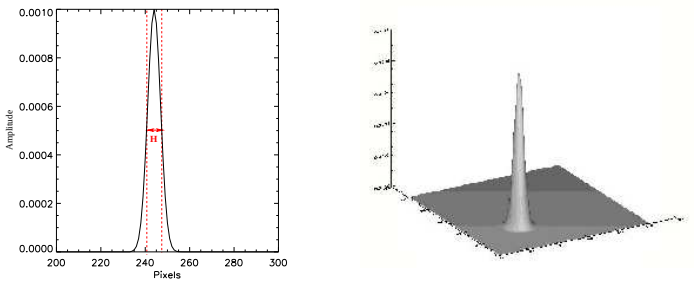

Figure 7. Numerical influence function f_i of the deformable mirror. Assumption: the wavefront deformation is a gaussian.

- We then translate this gaussian on the position of each actuators to get the NxN influence functions f_i of the deformable mirror.

4.1.2 Simulation of the interaction matrix

In numerical simulations, we assume that we do not know the response of the deformable mirror.

- We consider the NxN influence functions f_i of the deformable mirror (with i between 0 and $N^2 - 1$). We use the formalism presented in section 3 to estimate the deformation with the SCC. Hence, we get NxN estimated functions noted $f_{i,est}$. Figure 8 represents the estimation with the SCC of one influence function of the deformable mirror. We note that estimated function shows a cross structure around the gaussian estimated phase. This cross effect comes from the division by M in the estimator (Equation 28). While the phase and its estimator are rather alike (images 1 and 4 in Figure 5), for a random phase, it is not anymore the case for a influence function which is very localized phase defects.

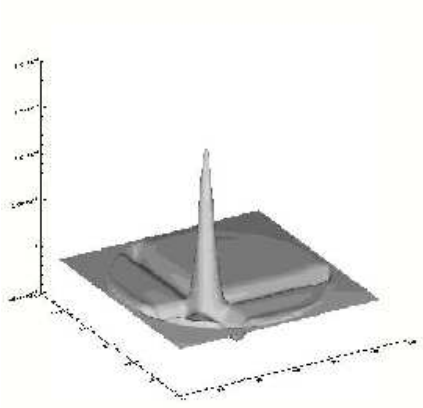

Figure 8. Numerical simulations - Estimation with the SCC of the wavefront deformation when one actuator is pulled ($f_{i,est}$).

- Some actuators are not inside the geometrical pupil and are useless for correcting aberrations. We then select the useful actuators which the SCC estimated deformation is larger than a treshold. We get $N1$ influence functions ($N1 < N^2$)
- We transform the estimated functions $f_{i,est}$ in vectors which fill the interaction matrix (Figure 9, left)

4.1.3 The synthetic interaction matrix

The string difference between f_i and $f_{i,est}$ introduced correlations between actuators on the same rows and columns than f_i. These correlations are completely fake. For this reason, the control matrix built on these $f_{i,est}$ proved to be rather inefficient to correct the phase. To overcome the cross effect, we build a synthetic interaction matrix from the experimental one.

- We consider the NxN influence functions of the deformable mirror. We select the estimated influence functions of the 10x10 central actuators.
- In order to avoid artefacts due to the FQPM coronagraph, we fit a gaussian on each SCC measurement $f_{i,est}$. Hence, we suppress the cross effect. We get 10x10 fitted gaussian functions noted G_i.
- On real data, the G_i are not identical and we create a single gaussian function G taking the median of the parameters.
- We translate G to every actuator position to build a NxN synthetic influence functions $f_{i,synt}$.
- We select useful actuators (as when creating the experimental interaction matrix) and we get N2 synthetic measurements ($N2 < N^2$).
- We transform these N2 synthetic measurements on vectors to create the synthetic interaction matrix (Figure 9, right).

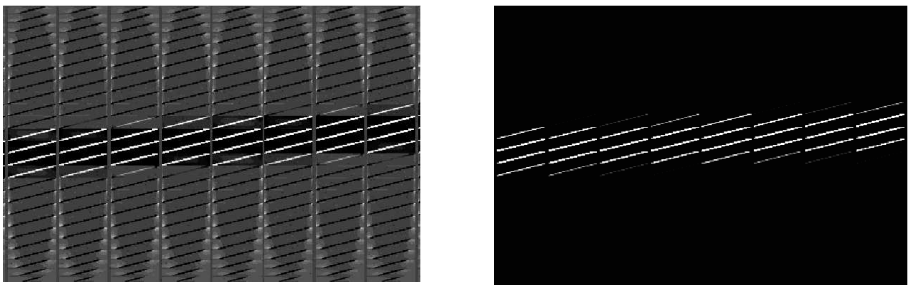

Figure 9. Left: Numerical interaction matrix created from $f_{i,est}$. Right: Synthetic interaction matrix.

4.1.4 The control matrix

As the interaction matrix is not squared it is not invertible, we use the method of minimum mean square to define the control matrix. Useful actuators have already been selected ($N2$ actuators selected, with $N2 < N^2$), so we do not filter any modes when creating this matrix. We note M_{int} and M_{com} interaction and control matrices respectively:

$$M_{com} = (M_{int}^T M_{int})^\dagger M_{int} \tag{31}$$

4.2 Performances

In the simulation, we consider a realistic case to reproduce phenomenon on the THD bench. In this section, we give the performance that we expect from numerical simulations for a single specific configuration that roughly reproduces the estimated defects and the characteristics of the laboratory testbed:

- Lyot stop diameter: $D_L = 98\% D_P$.
- Amplitude defects $\alpha = 9\%$, phase defects $\phi : 20$ nm rms (f^{-2} spectrum).
- Deformable mirror with N^2 actuators (with $N = 27$), square geometry.

In the simulation, we run 20 iterations of correction in order to get the best speckle suppression in the focal plane. Figure 10 represents the radial profile of images in the focal plane with respect to the angular separation. These profiles are the standard deviation in rings of $1\lambda/D$ width, divided to the maximum of the non-coronagraphic image. For the PSF, it is the mean intensity in the same rings instead of the standard deviation. The black curve represents the radial profile of the PSF, the red dotted curve corresponds to the SCC image (encoded speckles) before correction of phase and amplitude errors. The blue dashed dotted curve corresponds to the SCC image after phase and amplitude correction.

We define the contrast C at x λ/D_L as:

$$C(x) = \frac{\max(I_{nc})}{I(x)} \tag{32}$$

where I_{nc} is the non coronagraphic intensity distribution on the detector. In numerical simulation, we reach a contrast close to 2.10^7 between 5 and 10 λ/D_L. The estimation of the wavefront is done on a pupil which size is the Lyot stop size while the correction is done on the entire pupil. Hence, the correction is degraded in the edge of the pupil. As a consequence, low frequencies in the focal plane are less corrected as it can be seen on Figure 10. As the deformable mirror has a finite number of actuators, only speckles at frequencies smaller than the deformable mirror cut-off $\nu_c = N/(2D_P)$ can be corrected. The corrected zone of the deformable mirror depends on the number of actuators. Speckles are then only suppressed inside the corrected zone of the deformable mirror.

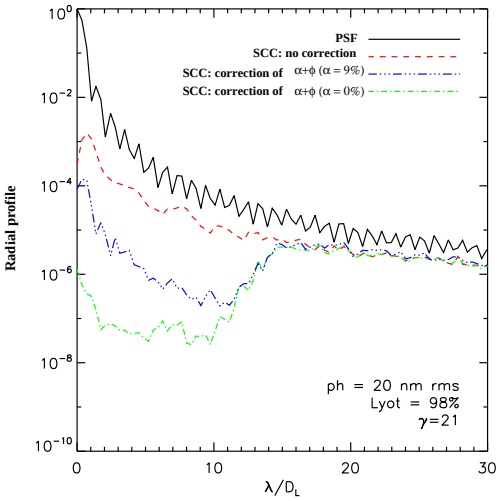

Figure 10. Radial profile of the simulated images in the focal plane with respect to the angular separation. Black curve: profile of the PSF. Red dotted line: profile of the SCC image before correction. Blue dotted-dashed curve: profile of the SCC image after phase and amplitude correction, ϕ: 20 nm rms, $\alpha = 9\%$ (20^{th} iteration of correction). Green dotted-dashed curve: profile of the SCC image after phase and amplitude correction, ϕ: 20 nm rms, $\alpha = 0\%$ (20^{th} iteration of correction)

5. EXPERIMENTAL SPECKLE SUPPRESSION WITH THE SCC ON THE THD BENCH

5.1 Description of the bench

The principle of the SCC has been tested and validated experimentally on the THD bench. Figure 11 shows the optical design of this bench. More details are given in Mas et al., 2010.[7]

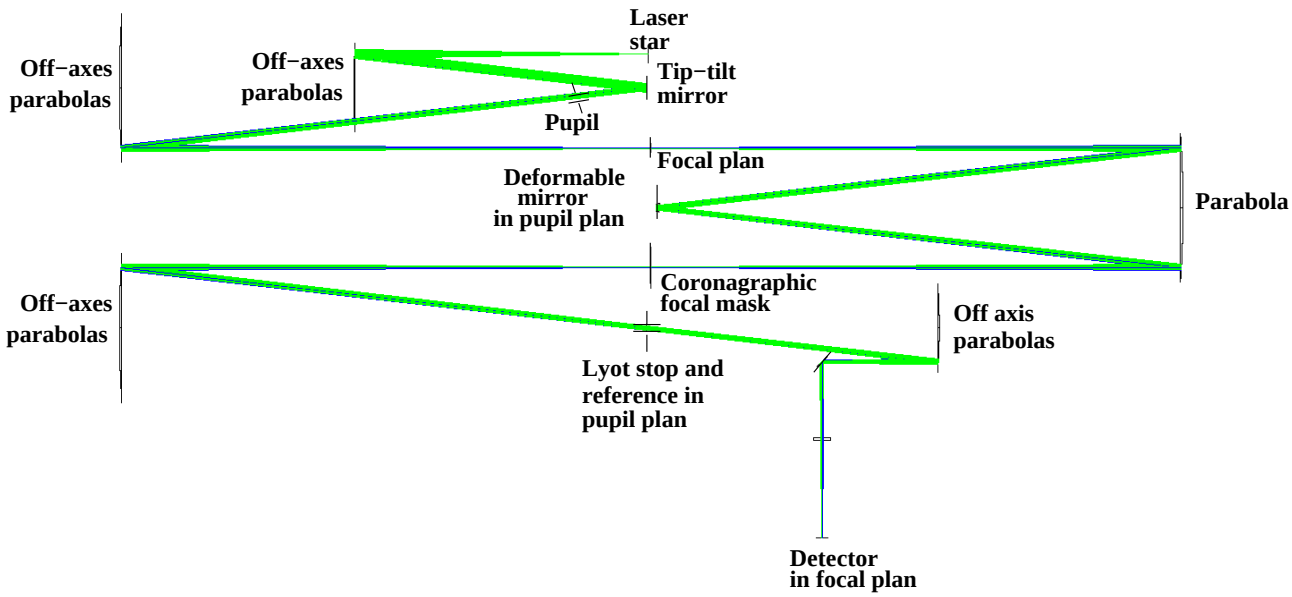

Figure 11. Optical design of the test bench THD.

We use a fibered laser beam ($\lambda = 635$ nm) to simulate the star. A tip-tilt mirror is located close to the first pupil plane. he diameter of the entrance pupil P is $D_P = 8.1$ mm. In the next pupil plane, we use an electrostatic deformable mirror from Boston Micromachines Society with 32x32 actuators to correct for aberrations upstream of the coronagraph. The FQPM coronagraph in the focal plane is monochromatic and optimized for $\lambda = 635$ nm. In the next pupil plane, the light is rejected out from the geometrical pupil and is stopped by the Lyot stop. We add the hole that creates the reference channel in this pupil plane. The Lyot stop diameter is $D_L = 8$ mm ($D_L \simeq 99\% D_P$) and the reference diameter is $D_R = 0.35$ mm. In the final focal plane, encoded speckles are recorded on a CCD.

5.2 Experimental results on speckle suppression

In this section, we show experimental results on speckle suppression using the SCC as a focal plane wavefront sensor. We create the synthetic interaction matrix from recorded data following the method presented in section 4.1.3. There is about 27x27 actuators in the pupil. The corrected zone of the deformable mirror is then, in the focal plane, a square area of $27\lambda/D_P$x$27\lambda/D_P$ if only phase errors upstream of the coronagraph are corrected. This zone is half smaller if we correct simultaneously phase and amplitude errors.[8] In the experiment, we first correct for phase errors, and then we correct phase and amplitude aberrations simultaneously. Figure 12 shows experimental SCC images in the focal plane before correction (image 1) after phase correction (image 2), and after phase and amplitude correction (image 3). Signature at high frequencies in the speckle pattern are induced

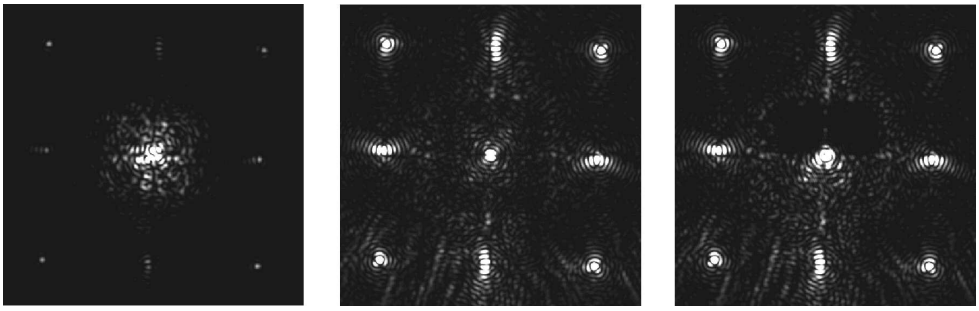

Figure 12. Experimental images in the focal plane. Image 1: SCC image before wavefront correction. Image 2: SCC image after phase correction. Image 3: SCC image after phase and amplitude correction.

by structures on the deformable mirror membrane. As these frequencies are higher than the cut-off frequency, this structure in the focal plane cannot be corrected.

In Figure 13, we present radial profile of experimental images in the focal plane. Black curve corresponds to the PSF, red dotted curve corresponds to the SCC image before correction, light blue curve corresponds to SCC image after phase correction, and dark blue curve after phase and amplitude correction. On this plot, we can see the cut-off of the deformable mirror around $12\lambda/D_L$ ($\simeq 13\lambda/D_P$). With this experiment, we succeed reaching a contrast close to 10^7 between 5 and 11 λ/D_L.

From numerical simulations, we expect a contrast close to 2.10^7 in the same area (Figure 10). The small difference is mainly due to the high frequency structure of the deformable mirror membrane that we do not take into account for the numerical simulations.

6. CONCLUSION

We demonstrated that the SCC can be used as a focal plane wavefront sensor to estimate phase and amplitude errors upstream of a FQPM coronagraph directly from the final science image. We developed the formalism to find a linear estimator of the wavefront. We then presented the method to build a synthetic interaction matrix taking into account effects of the FQPM coronagraph on the SCC wavefront measurements. From numerical simulations and assuming 9% amplitude aberrations and 20 nm rms phase errors, we expect to reach a contrast close to 2.10^7 in the focal plane between 5 and 11 λ/D_L simulating a deformable mirror with 27x27 actuators. Using such a deformable mirror on our high contrast imaging test bench, we reached a contrast close to 10^7

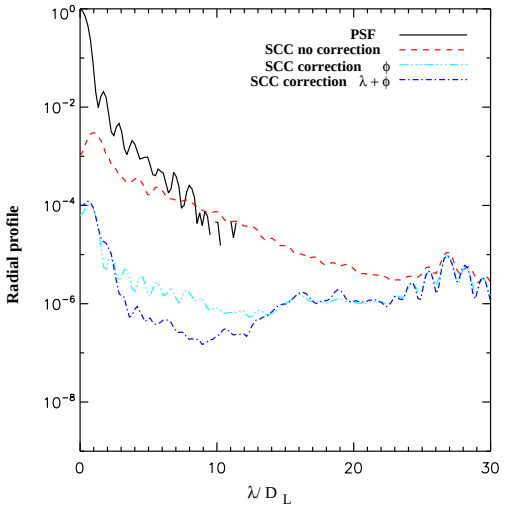

Figure 13. Radial profile of the experimental images in the focal plane with respect to the angular separation. Black curve: profile of the PSF. Red dotted line: profile of the SCC image before correction. Blue light dotted-dashed curve: profile of the SCC image after phase correction. Blue dotted-dashed curve: profile of the SCC image after phase and amplitude correction.

between 5 and 11 λ/D_L in the focal plane, on the bench. Correcting the phase and ampitude using the estimator we presented in this paper the first step of our experimental demonstration. We are now working on more advanced estimator and correcting procedures that allow us to reach higher contrast ($\simeq 10^8$) as shown in Baudoz et al., 2012.[9]

REFERENCES

[1] Baudoz, P., Boccaletti, A., Baudrand, J., Rouan, D., 2006. The Self-Coherent Camera: a new tool for planet detection. *IAU Colloq. 200: Direct Imaging of Exoplanets: Sciences Techniques*, 553-558

[2] Galicher, R. & Baudoz, P., 2007. Expected performance of a self-coherent camera. *Comptes Rendus Physique*, **8**, 333-339

[3] Galicher, R., Baudoz, P., Rousset, G., 2008. Wavefront error correction and Earth-like planet detection by self-coherent camera in space. *A&A*, **488**, L9-L12

[4] Galicher, R., Baudoz, P., Rousset, G., Totems, J., Mas, M., 2010. Self-coherent camera as a focal plane wavefront sensor: simulations. *A&A*, **530**, A31+

[5] Mazoyer, J., Baudoz, P., Mas, M., Rousset, G., Galicher, R., 2012. Experimental parametric study of the Self-Coherent Camera. *Society of Photo-Optical Instrumentation Engineers (SPIE) Conference Series*, 8442

[6] Abe, L., Dominiciano de Sousa, A. Jr., Vakili, F., and Gay, J., 2003. Phase Knife Coronagraph - II Laboratory results, *Astronomy and Astrophysics* **400**, 385-392

[7] Mas, M., Baudoz, P., Rousset, G., Galicher, R., Baudrand, J., 2010. The Self-Coherent Camera: first results of a high contrast imaging bench in visible light. *Society of Photo-Optical Instrumentation Engineers (SPIE) Conference Series*, 7735

[8] Bordé, P., Traub, W., A., 2006. High-Contrast Imaging from Space: Speckle Nulling in a Low-Aberration Regime. *ApJ*, **638**,488-498

[9] Baudoz, P., Mazoyer, J., Rousset, G., Mas, M., Galicher, R., 2012. Dark hole and planet detection: laboratory results using the Self-Coherent Camera. *Society of Photo-Optical Instrumentation Engineers (SPIE) Conference Series*, 8446